

# In Situ Solid–Gas Reactivity of Nanoscaled Metal Borides from Molten Salt Synthesis

Guillaume Gouget,<sup>†,‡</sup> Damien P. Debecker,<sup>▼,§</sup> Ara Kim,<sup>†,▼</sup> Giorgia Olivieri,<sup>⊥</sup> Jean-Jacques Gallet,<sup>⊥,||</sup> Fabrice Bournel,<sup>⊥,||</sup> Cyril Thomas,<sup>▼,§</sup> Ovidiu Ersen,<sup>#</sup> Simona Moldovan,<sup>||,¶</sup> Clément Sanchez,<sup>†</sup> Sophie Carencu,<sup>†</sup> and David Portehault<sup>\*,†,§</sup>

<sup>†</sup>Sorbonne Universités-UPMC Univ. Paris 06, CNRS, Collège de France, Laboratoire de Chimie de la Matière Condensée de Paris, 4 place Jussieu, F-75252 Paris Cedex 05, France

<sup>▼</sup>Université Catholique de Louvain, Institute of Condensed Matter & Nanosciences, Molecules, Solids & Reactivity, Place Louis Pasteur 1, 1348 Louvain-la-Neuve, Belgium

<sup>⊥</sup>Synchrotron SOLEIL L'Orme des Merisiers, Saint-Aubin, BP 48, 91192 Gif sur Yvette Cedex, France

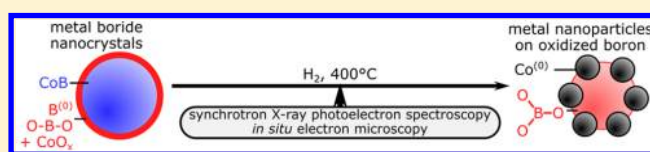
<sup>||</sup>Sorbonne Universités, UPMC Univ. Paris 06, Laboratoire de Chimie Physique, Matière et Rayonnement, 4 place Jussieu, F-75252 Paris Cedex 05, France

<sup>§</sup>Sorbonne Universités, UPMC Univ. Paris 06, CNRS, Laboratoire de Réactivité de Surface, 4 place Jussieu, F-75252 Paris Cedex 05, France

<sup>#</sup>Institut de Physique et Chimie des Matériaux de Strasbourg, CNRS, 23 Rue Loess, BP 43, F-67034 Strasbourg, France

## Supporting Information

**ABSTRACT:** Metal borides have mostly been studied as bulk materials. The nanoscale provides new opportunities to investigate the properties of these materials, e.g., nanoscale hardening and surface reactivity. Metal borides are often considered stable solids because of their covalent character, but little is known on their behavior under a reactive atmosphere, especially reductive gases. We use molten salt synthesis at 750 °C to provide cobalt monoboride (CoB) nanocrystals embedded in an amorphous layer of cobalt(II) and partially oxidized boron as a model platform to study morphological, chemical, and structural evolutions of the boride and the superficial layer exposed to argon, dihydrogen (H<sub>2</sub>), and a mixture of H<sub>2</sub> and carbon dioxide (CO<sub>2</sub>) through a multiscale in situ approach: environmental transmission electron microscopy, synchrotron-based near-ambient-pressure X-ray photoelectron spectroscopy, and near-edge X-ray absorption spectroscopy. Although the material is stable under argon, H<sub>2</sub> triggers at 400 °C decomposition of CoB, leading to cobalt(0) nanoparticles. We then show that H<sub>2</sub> activates CoB for the catalysis of CO<sub>2</sub> methanation. A similar decomposition process is also observed on NiB nanocrystals under oxidizing conditions at 300 °C. Our work highlights the instability under reactive atmospheres of nanocrystalline cobalt and nickel borides obtained from molten salt synthesis. Therefore, we question the general stability of metal borides with distinct compositions under such conditions. These results shed light on the actual species in metal boride catalysis and provide the framework for future applications of metal borides in their stability domains.



## INTRODUCTION

Synthetic routes toward nanocrystalline metal borides are drawing increasing interest<sup>1–8</sup> because of the properties of these materials, which differ from those of other solids, including magnetism, plasmonics, thermoelectricity, superconductivity, and superhardness.<sup>2,9–18</sup> Nanoscaled metal borides are also attractive as heterogeneous catalysts of the selective hydrogenation of various functional organic groups.<sup>8,19,20</sup> Moreover, cobalt, nickel, iron, and palladium borides<sup>8</sup> are currently considered for the production of hydrogen, by catalysis of the hydrolysis of sodium borohydride (NaBH<sub>4</sub>)<sup>21,22</sup> and electrocatalysis of the hydrogen evolution reaction.<sup>23–26</sup> In all cases, the nanoscale provides a parameter to influence or enhance properties, but it has been only scarcely explored because of the difficulty in synthesizing nanoscaled

metal borides. Assessing the chemical stability and structural evolution of these nanomaterials is of utmost importance to identify suitable temperature ranges for operation as thermoelectric materials, hard coatings, or heterogeneous catalysts, for instance.<sup>22,27</sup> Such applications require chemical and thermal stability that is not met by readily available amorphous boride nanoparticles but should be strongly improved in crystalline nanoparticles. Although the stability of borides under air and inert atmospheres has been examined,<sup>1,13,28–31</sup> compositional, structural, and morphological evolutions of nanocrystalline metal borides in contact with other gases, especially the reductive atmosphere encountered in catalytic processes, are

Received: May 19, 2017

Published: July 24, 2017

unknown because of the scarcity of crystalline boride nanomaterials.<sup>1–8</sup>

Herein we use inorganic molten salts as media to synthesize crystalline cobalt and nickel monoboride (CoB and NiB) nanoparticles embedded in an amorphous layer comprising cobalt(II) species and partially oxidized boron.<sup>5,6</sup> We then explore the reactivity of these nanomaterials, exposing high surface areas. Our multiscale in situ analytical methodology combines two techniques enabling studies under reactive atmospheres. First, environmental transmission electron microscopy (TEM) enables one to investigate the nanoscale morphology evolution at pressures of up to 1 bar.<sup>32,33</sup> Second, ensembles of nanoparticles are analyzed by synchrotron-based near-ambient-pressure X-ray photoelectron spectroscopy (NAP-XPS)<sup>34</sup> and near-edge X-ray absorption spectroscopy (NEXAFS) to provide information on chemical and structural evolutions occurring at the surface and in the core of the material, respectively, under a few millibars of several gases, especially hydrogen. On CoB, we demonstrate that the boride is surprisingly decomposed under reducing conditions, yielding cobalt particles at a relatively low temperature of 400 °C. We then show that hydrogen treatment activates CoB for the catalysis of carbon dioxide (CO<sub>2</sub>) methanation, through these cobalt(0) species. Similar decomposition occurs in NiB nanocrystals exposed to oxidizing conditions, suggesting that this behavior may be generalized to many other metal boride nanomaterials under a reactive atmosphere, thus providing the frame for their future use as catalysts and functional coatings.

## RESULTS AND DISCUSSION

**CoB Nanoparticles Synthesized in Molten Salts.** CoB nanocrystals were synthesized under argon at 750 °C from the reaction between cobalt(II) chloride (CoCl<sub>2</sub>) and NaBH<sub>4</sub> in a lithium chloride (LiCl)/potassium chloride (KCl) mixture (45/55 wt %; melting point of 353 °C). After cooling to room temperature (RT), the frozen salt medium was washed with deionized water. A black powder was recovered and stored in air.

X-ray diffraction (XRD; Figure 1a) shows that CoB is the only crystalline phase. The apparent size is  $14 \pm 2$  nm according to the Scherrer formula. TEM and high-resolution TEM (HRTEM; Figure 1b,c) reveal that the sample is composed of single-crystal CoB nanoparticles with diameters ranging from 4 to 20 nm, in agreement with XRD. These particles are smaller than any other CoB nanoparticles reported in the literature to date (18–22 nm).<sup>35</sup> The particles are dispersed in an amorphous matrix exhibiting a lower contrast and a 2–5 nm thickness. High-contrast inclusions of ca. 1 nm (black arrows in Figure 1b) are detected in the amorphous matrix. Z-contrast pictures acquired by high-annular-angle dark-field detection in scanning TEM mode (STEM-HAADF; Figure 1d) highlight cobalt-rich regions as bright areas corresponding to the CoB nanoparticles and to subnanometric cobalt-rich inclusions in the amorphous layer. These latter species are not detected by XRD. Energy-dispersive X-ray analysis indicates that cobalt, boron, and oxygen are the only elements present in the material (data not shown). The measured composition of Co<sub>0.30</sub>B<sub>0.53</sub>O<sub>0.17</sub> is in accordance with the Co/B ratio of 0.6 measured by inductively coupled plasma (ICP). On the basis of a previous study, oxygen is expected to be located in the amorphous matrix.<sup>5</sup> Brunauer–Emmett–Teller analysis of the dinitrogen sorption isotherms indicates a

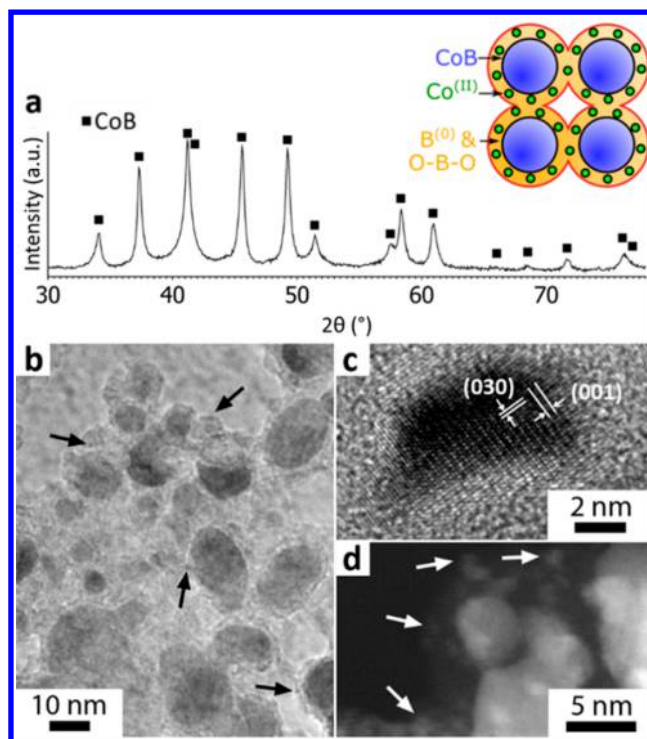


**Figure 1.** (a) Powder XRD pattern of a CoB sample synthesized in inorganic molten salts at 750 °C for 1.5 h. Scheme of the sample nanostructure deduced from XRD, TEM, and XPS. (b) TEM picture of CoB nanoparticles embedded in an amorphous matrix. Black arrows highlight subnanometer inclusions in the matrix. (c) HRTEM picture of a CoB nanoparticle. (d) Z-contrast picture from STEM-HAADF. White arrows indicate bright cobalt-rich inclusions in the superficial layer.

specific surface area of  $71 \text{ m}^2 \text{ g}^{-1}$ , more than twice the highest value reported in the literature ( $32 \text{ m}^2 \text{ g}^{-1}$ ) for CoB materials.<sup>36</sup>

Compositional information on the superficial amorphous layer was further provided by XPS under ultrahigh vacuum (UHV; Figure 2). Using synchrotron-based radiation (TEMPO beamline at Synchrotron SOLEIL, Gif sur Yvette Cedex, France) enabled changing of the inelastic mean-free path of the photoelectron, and, hence, the depth of analysis,<sup>37–39</sup> by varying the incident photon energy (IPE):<sup>40–42</sup> 1.7 nm for O 1s and B 1s photoelectrons (IPE 1050 and 725 eV, respectively); 1.1 and 2.1 nm for Co 2p<sub>3/2</sub> photoelectrons (IPE 1050 and 1500 eV, respectively). Under IPE 1500 eV, the Co 2p<sub>3/2</sub> region shows a peak at 778.4 eV attributed to CoB<sup>43</sup> and accompanied by a broad signal between 776 and 785 eV characteristic of cobalt(II).<sup>44</sup> The O 1s contribution at 532.0 eV is consistent with oxidized cobalt species, confirming the oxygen environment surrounding cobalt(II). The O 1s contribution at 533.0 eV corresponds to oxygen species linked to boron in agreement with the B 1s contribution at 193.0 eV,<sup>45</sup> attributed to partially oxidized boron(II). The two other B 1s contributions at 189.2 and 187.9 eV correspond to elemental boron (B<sup>0</sup>) and CoB,<sup>43</sup> respectively. The high binding energy (BE) for B<sup>0</sup> compared to the reported values<sup>22,45</sup> is due to the nanostructure that yields charge effects.<sup>46</sup> CoB is detected in the B 1s region but also in the Co 2p<sub>3/2</sub> region for a photon energy of 1500 eV. At a lower photon energy of 1050 eV probing a thinner layer of ca. 1.1 nm, cobalt(II) is the only species detected in the Co 2p<sub>3/2</sub> region, with peaks more resolved than those at a photon energy of 1500 eV: 779.3 eV

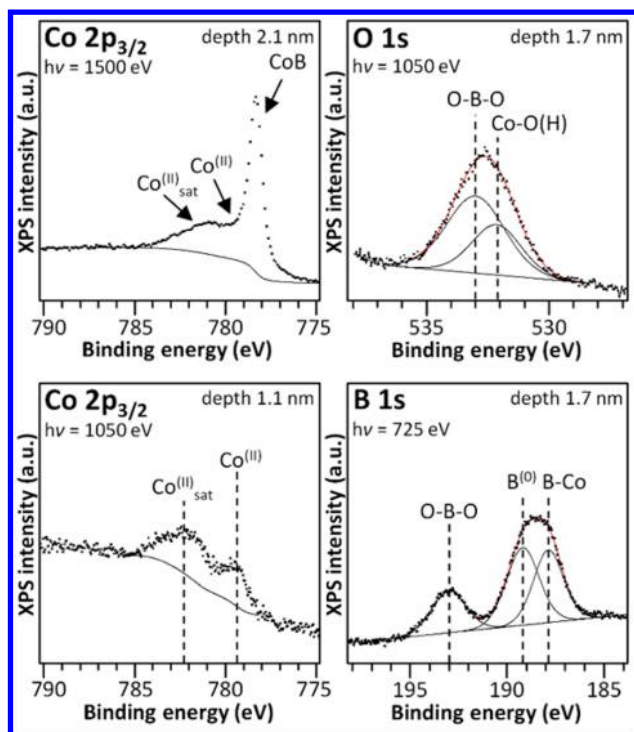


**Figure 2.** UHV-XPS spectra of the CoB nanocomposite in the Co  $2p_{3/2}$ , O  $1s$ , and B  $1s$  regions in the initial state.  $h\nu$  = photon energy. The approximate depths of analysis are also given.

and a broader satellite at 782.5 eV (Figure 2).<sup>44</sup> These XPS data provide strong support to XRD and STEM-HAADF analyses, showing that molten-salt-derived CoB is a nanocomposite made of CoB nanocrystals buried below a ca. 2-nm-thick amorphous layer, composed of partially oxidized amorphous boron ( $B^0$  and  $BO_2$  species) and cobalt oxide and/or (oxyhydr)oxide inclusions (scheme in Figure 1).

Because the synthesis was performed in oxygen-free conditions, the oxidized boron and cobalt(II) species in the amorphous layer originate from exposure of the material to water during the washing step and air during storage. Interestingly, the cobalt(II) species may be interesting precursors to cobalt(0) catalysts, especially for carbon monoxide (CO) or  $CO_2$  methanation, like cobalt oxides.<sup>47</sup> We thus explore in the following parts how a catalyst activation procedure, namely, reduction under hydrogen gas, impacts the nanostructure and local structure of the material. Then, as an example, we examine how a typical gas reagent mixture used for methanation [dihydrogen ( $H_2$ )/ $CO_2$ ] can impact the activated material.

Both morphological and compositional evolutions were characterized using (i) environmental STEM with Z-contrast HAADF imaging, (ii) XPS under UHV and NAP conditions, which is sensitive only to modifications of the superficial layer (1–2 nm), and (iii) NEXAFS for a complementary spectroscopic characterization to a depth of approximately 10 nm, i.e., comprising the CoB nanocrystals. Although there is a pressure gap between environmental TEM (1 bar) and NAP-XPS/NEXAFS (a few millibars), in the latter case, the material surface is fully saturated with adsorbates, thus providing relevant information on the actual state under higher pressure.<sup>48–51</sup>

**Morphology Evolution of Nanoscaled Cobalt Boride under  $H_2$ .** STEM (Figure 3, left) and STEM-HAADF (Figure

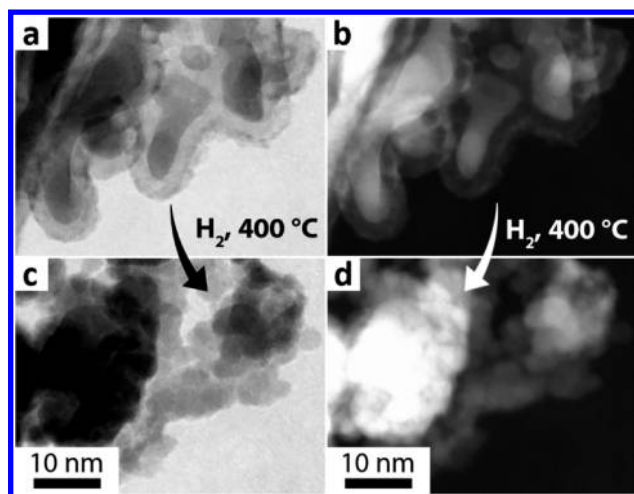


**Figure 3.** In situ STEM (left) and STEM-HAADF (right) images of the nanocomposite under different conditions: (a and b) under 0.3 bar of argon at 150 °C; (c and d) under 0.9 bar of  $H_2$  at 400 °C. The four micrographs are taken from the same region with an identical scale.

3, right) images of the nanocomposite powder were recorded under environmental conditions. Under 0.3 bar of argon at 150 °C (Figure 3a,b), the morphological characteristics of the powder are similar to those of the pristine sample (Figure 1): CoB nanoparticles are surrounded by the amorphous layer containing cobalt-rich inclusions. The same region is observed under reducing conditions (Figure 3c,d). Upon exposure to 0.9 bar of  $H_2$  at 400 °C, core-shell particles reorganize into nanoparticles with homogeneous contrast, thus demonstrating strong morphological reconstruction of the initial crystalline particles (Figure S1), with fragmentation into smaller nanoparticles. Chemical and structural evolutions accompanying these morphological changes under reactive gases were then investigated using XPS.

**Surface Reactivity of Nanoscaled Cobalt Boride under Hydrogen.** XPS under UHV conditions was performed on the CoB powder after exposure to a static atmosphere of 1 bar of pure  $H_2$  at 400 °C (Figure 4). The spectra in the Co  $2p_{3/2}$ , O  $1s$ , and B  $1s$  regions were recorded with photon energies of 1050, 725, and 725 eV, respectively, corresponding to approximate depths of analysis of 1.1, 0.9, and 1.7 nm. The Co  $2p_{3/2}$  region shows one peak at  $\sim 779.0$  eV corresponding to reduced cobalt, in accordance with the absence of (H)O–Co species in the O  $1s$  region.<sup>52</sup> One single peak is detected in the B  $1s$  region at 195.4 eV. Similarly, in the O  $1s$  region, one single peak is detected at 535.0 eV. Both signals correspond to fully oxidized boron. Compared to the usual BEs assigned to oxidized boron in previous literature data, they are shifted by 1.8 eV to higher BEs.<sup>53</sup> This discrepancy may originate from charge effects due to the nanostructure. Compared to the initial material in the B  $1s$  region, no  $B^0$  or  $B^{II}$  is observed after  $H_2$  treatment.

**Surface Reactivity of Nanoscaled Cobalt Boride under a Mixture of  $H_2$  and  $CO_2$ .** The nanomaterial treated under 1 bar of  $H_2$  at 400 °C and then analyzed by XPS under UHV conditions was exposed to a  $H_2/CO_2$  gas mixture (4:1 volume ratio) at 400 °C during analysis. To enable NAP-XPS acquisition (Figure 4), the pressure in the chamber was kept at 2 mbar. Boron remains fully oxidized, as shown by the B  $1s$  and O  $1s$  contributions at 195.4 and 534.8 eV, respectively. The absence of a peak at lower BEs in the B  $1s$  region indicates

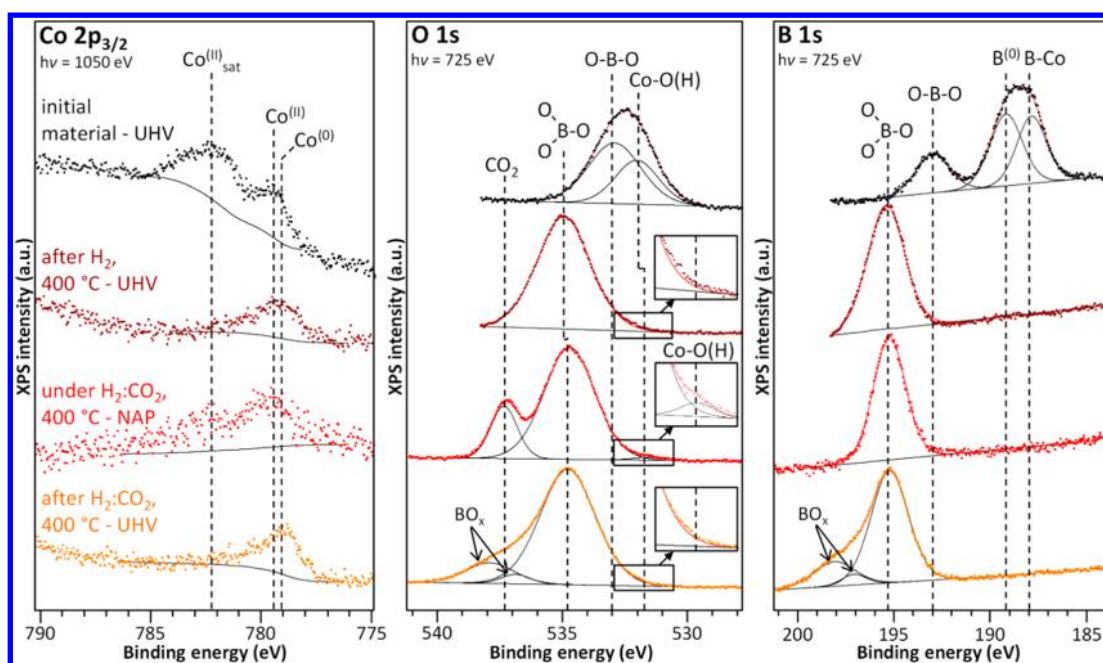


**Figure 4.** XPS spectra in the Co  $2p_{3/2}$ , O  $1s$ , and B  $1s$  regions of the CoB nanocomposite. From top to bottom: initial state under UHV; after exposure to 1 bar of  $H_2$  at 400 °C under UHV; near-ambient-pressure conditions of 2 mbar of  $H_2/CO_2$  (4:1 volume ratio) at 400 °C; under UHV at RT after exposure to  $H_2/CO_2$  (4:1 volume ratio) at 400 °C.  $h\nu$  = photon energy.

that neither CoB nor elemental and partially oxidized boron is present on the surface of the material (depth of analysis of 1.7 nm). In the O  $1s$  region, the contribution at 537.4 eV corresponds to gas-phase  $CO_2$ . The shoulder of weak intensity at 532.0 eV is ascribed to (H)O–Co species (inset). In the Co  $2p_{3/2}$  region, the broad satellite of oxidized cobalt is detected between 781 and 785 eV, despite a poor signal-to-noise ratio due to the gas phase absorbing most of the emitted photoelectrons. Oxidized cobalt species thus form on the surface of the material when exposed to  $H_2/CO_2$  at 400 °C.

Back to RT and under UHV conditions (Figure 4), the signal in the Co  $2p_{3/2}$  region shows the exclusive presence of metallic cobalt, while the shoulder at 532.0 eV in the O  $1s$  region disappears. Thus, the (H)O–Co species formed under NAP conditions are not stable under UHV conditions, and fully reduced cobalt species are restored, as observed after exposure to 1 atm of pure  $H_2$  at 400 °C (Figure 4). Note that two additional species (“ $BO_x$ ” in Figure 4) are detected. They are attributed to UHV-specific species and not representative of the material exposed to environmental conditions (discussion in the Supporting Information and Figure S2). All in all, zerovalent cobalt species are formed on the surface of the material initially composed of partially oxidized boron and  $Co^{II}$  species. The contribution of deeper CoB in the B  $1s$  region also disappears, but the changes of the monoboride core cannot be fully assessed using XPS. Indeed, XPS is only able to probe the first 1–2 nm beneath the surface. Hence, to probe the core of the material, especially the CoB nanoparticles buried under the superficial layer, we have performed NEXAFS on the same synchrotron beamline and the same materials as XPS measurements, also in NAP conditions. The total electron yield mode of NEXAFS was used to provide a depth of analysis of ca. 10 nm, 1 order of magnitude deeper than that of XPS.<sup>54,55</sup>

**Core Reactivity of Nanoscaled Cobalt Boride under  $H_2$  and a  $H_2/CO_2$  Mixture.** NEXAFS spectra have been recorded

to probe both crystalline nanoparticles and the amorphous component (analysis depth  $\sim 10$  nm) at the Co L-edge, O K-edge, and B K-edge (Figure 5). The spectra for the initial state show contributions of CoB, oxidized and nonoxidized (broad signal) of amorphous boron, and oxidized cobalt inclusions. Hence, NEXAFS confirms the conclusions obtained from XRD, TEM, and XPS: the initial material is constituted of CoB nanocrystals embedded in a  $\sim 2$ -nm-thick amorphous layer, containing cobalt(II) in the form of oxides or (oxyhydr)oxides (scheme in Figure 1), dispersed in partially oxidized boron, with  $BO_2$ ,  $BO_3$ , and  $B^0$  species. Between the initial state and the sample exposed to  $H_2$  at 400 °C, the contributions of oxidized cobalt<sup>56</sup> and elemental boron<sup>55</sup> have disappeared, in agreement with UHV-XPS. NEXAFS thus confirms that the whole CoB core is converted into oxidized boron and metallic cobalt after exposure to the reducing atmosphere. NEXAFS spectra of the sample under  $H_2/CO_2$  (NAP conditions) at 400 °C are also displayed. Although poorer signal-to-noise ratios are obtained, they are similar to those in the spectra after the reducing treatment. This indicates that no further change happens in the core of the material upon exposure to the  $H_2/CO_2$  mixture, in agreement with XPS.

In brief, combined TEM, XPS, and NEXAFS studies demonstrate that the oxidized cobalt inclusions in the superficial layer, as well as the CoB nanoparticles, are converted into metallic cobalt nanoparticles during a  $H_2$  pretreatment, while boron is further oxidized by surrounding oxygen species initially bound to cobalt and possibly adsorbed water molecules. After the reducing treatment, the compositional homogeneity between the initial core and superficial layer observed by XPS and NEXAFS is in accordance with the TEM observations: core–shell nanoparticles turning to homogeneously contrasted ones.

**Reactivity of Nanoscaled Nickel Boride under Hydrogen and a Mixture of  $H_2$  and Dioxygen ( $O_2$ ).** To assess the generality of the structural modifications evidenced on CoB

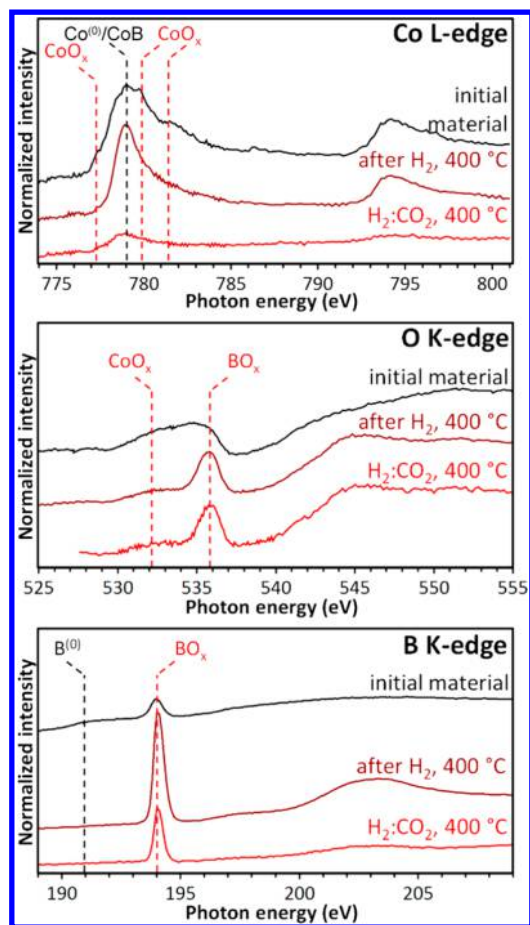


**Figure 5.** NEXAFS spectra at the Co L-edge, O K-edge, and B K-edge. From top to bottom: the initial CoB nanocomposite under UHV; after exposure to 1 bar of  $\text{H}_2$  at 400 °C under UHV; near-ambient-pressure conditions with 2 mbar of  $\text{H}_2/\text{CO}_2$  (4:1 volume ratio) at 400 °C.

upon exposure to a reactive gas atmosphere, NiB was investigated. The nanoparticles were synthesized using the same inorganic molten salt route. The NiB nanocomposite is described in detail elsewhere.<sup>6</sup> This material is made of NiB nanocrystals surrounded by an amorphous layer. The XRD

pattern of the as-obtained powder highlights the presence of NiB crystallites with apparent sizes of  $9 \pm 2 \text{ nm}$ <sup>6</sup> together with traces of  $\text{Ni}_4\text{B}_3$  (Figure 6b, top). In contrast to CoB, it has been shown recently by TEM that no nickel atom resides in the superficial amorphous layer<sup>6</sup> and that all the nickel atoms are involved in NiB. The NiB nanoparticles are exposed consecutively to reducing and oxidizing conditions at 1 atm. The different steps are schematized in Figure 6a. Chromatography analysis of the exhaust gas does not show any  $\text{H}_2$  consumption during all reducing steps (not shown). Oxygen depletion from 320 to 420 °C during the first oxidation step (Figure 6c) indicates oxidation of the nanocomposite. No further  $\text{O}_2$  consumption is observed in the subsequent oxidizing steps (Figure 6d), despite the intermediate reducing treatments. The first oxidation process is thus irreversible. After subsequent cycles, the NiB black powder turns into a black monolith and a white powder deposits onto the reactor walls. The XRD pattern of the monolith highlights the presence of metallic nickel and traces of  $\text{Ni}_3\text{B}$  instead of the parent NiB and  $\text{Ni}_4\text{B}_3$  (minor amount) material (Figure 6b, bottom). The resulting nickel particles exhibit a crystallite size of ca. 30 nm. Segregation of nickel and boron can then be correlated to boron oxidation during the first oxidation treatment. The O/B molar ratio is 1.5 according to  $\text{O}_2$  consumption in the first oxidation step, in good agreement with the expected stoichiometry of  $\text{B}_2\text{O}_3$ . The white powder deposited on the reactor walls is therefore  $\text{B}_2\text{O}_3$ , which is known to melt at 450 °C and shows high volatility in this temperature range.<sup>57</sup>

#### Catalysis of $\text{CO}_2$ Methanation over CoB-Derived Cobalt Nanoparticles.

In situ studies shown above demonstrate that exposure to  $\text{H}_2$  at 400 °C triggers phase segregation of CoB into oxidized boron and cobalt(0), a typical catalyst of carbon (di)oxide methanation. Hence, we assessed the catalytic activity of our CoB material toward  $\text{CO}_2$  methanation. The material was deposited on  $\text{TiO}_2$ -P25 Degussa (mixture of 20–50 nm rutile/anatase titania nanoparticles in a 20/80 mass ratio; specific surface area of about  $60 \text{ m}^2 \text{ g}^{-1}$ ) as a support already used for  $\text{CO}_2$  methanation.<sup>58,59</sup> The supported material (10 wt %) was treated in situ under  $\text{H}_2$  (1 atm) at 400 °C for 2 h and then exposed to a  $\text{H}_2/\text{CO}_2$ /helium mixture with a 4:1:5 volume ratio at 1 atm. The gas outlet was analyzed by

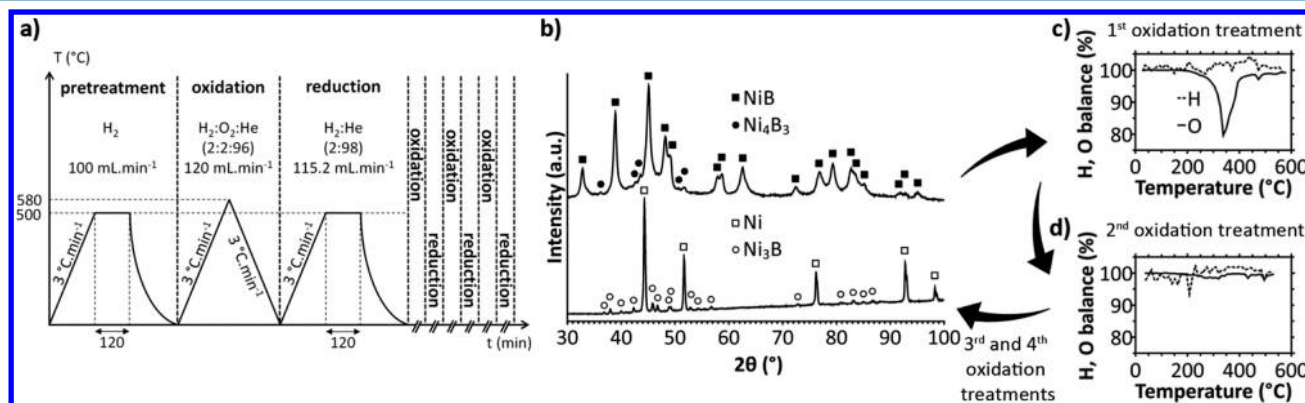


**Figure 6.** Destabilization of NiB nanoparticles during reduction and oxidation treatments. (a) Consecutive treatments under gases. The oxidation–reduction treatment was repeated four times. (b) XRD patterns of a sample composed of NiB nanoparticles (top) synthesized in inorganic molten salts at 750 °C for 1.5 h and the sample after the reducing–oxidizing treatments (bottom). (c and d) Elemental hydrogen and oxygen balances during the two first consecutive oxidizing heat treatments of NiB nanoparticles:  $\text{H}_2/\text{O}_2$ /helium mixture (2:2:96 volume ratio) to 580 °C at  $3 \text{ }^\circ\text{C min}^{-1}$ . Two oxidizing treatments are separated by exposure to  $\text{H}_2$ /helium (2:98 volume ratio) at 500 °C for 2 h, not showing any consumption of hydrogen (not shown). Elemental balances during the third and fourth oxidation treatments are similar to that shown in part d.

gas-phase chromatography. No species other than methane ( $\text{CH}_4$ ) and those present in the gas feed were detected.

The  $\text{CH}_4$  production rate measured after 20 min on stream strongly depends on the temperature (Figure S3). It is maximized between 400 and 500 °C. Figure 7 shows the

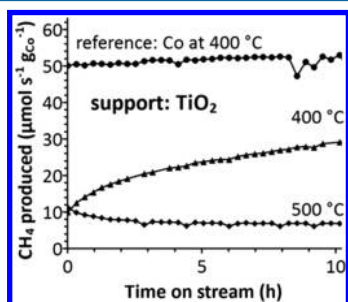


**Figure 7.**  $\text{CH}_4$  production rate as a function of the time on stream for  $\text{TiO}_2$ -supported CoB at 400 and 500 °C. The behavior of a Co/ $\text{TiO}_2$  reference sample is also shown for comparison. Inner gas mixture:  $\text{H}_2/\text{CO}_2$ /helium (4:1:5 volume ratio), 1 atm, 20 mL  $\text{min}^{-1}$ . Pretreatment:  $\text{H}_2$ , 1 atm, 30 mL  $\text{min}^{-1}$  at 400 °C for 2 h.

$\text{CH}_4$  production rate as a function of the time on stream at 400 and 500 °C. Deactivation occurs at 500 °C, but the behavior at 400 °C is drastically different: the  $\text{CH}_4$  production rate continuously increases during the whole experiment. Increases of 2- and 3-fold are observed after 2 and 10 h on stream, respectively. Note that, after 10 h on stream, the production rate of  $\text{CH}_4$  has not yet reached a steady state, but it is still increasing over ca. 30 mol  $\text{s}^{-1}$   $\text{g}_{\text{Co}}^{-1}$ . In comparison, a reference Co/ $\text{TiO}_2$ -P25 sample with the same cobalt content, formed by wet impregnation of  $\text{Co}_3\text{O}_4$  supported on titania,<sup>60</sup> shows a constant  $\text{CH}_4$  production rate of 50 mol  $\text{s}^{-1}$   $\text{g}_{\text{Co}}^{-1}$ . Activation of the CoB sample with time on stream at 400 °C therefore indicates that significant modifications of the catalyst occur, with the activity trend toward the behavior of cobalt, in accordance with the structural evolutions described in the previous sections. To confirm such changes,  $\text{TiO}_2$ -supported CoB materials have been extracted after each step of the catalysis test (Figure S4). Indeed, powder XRD patterns show phase segregation from CoB to cubic cobalt. The generality of the decomposition process has been confirmed by using silica as an alternative support (Figures S5 and S6).

**Instability of Metal Borides Exposed to Reactive Atmospheres.** The experiments reported above clearly demonstrate both chemical and morphological changes of the CoB-based nanocomposite due to exposure to  $\text{H}_2$ . These changes are schematized in Figure 8. In the superficial amorphous layer, the formation of cobalt nanoparticles occurs through borothermal reduction: reduction of cobalt(II) oxides

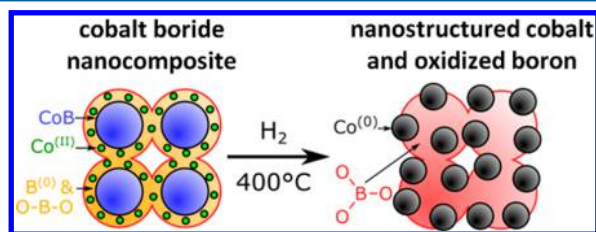


**Figure 8.** Chemical and morphological modifications of the CoB nanocomposite upon exposure to  $\text{H}_2$ .

and/or (oxyhydr)oxides by the initially present elemental boron and partially oxidized boron species.

In the core, elemental segregation leads to metallic cobalt, while boron is oxidized either in boron oxide or in boric acid. Heat treatments of amorphous cobalt–boron thin films under various atmospheres were shown by Patel et al. to lead to metallic cobalt only under pure  $\text{O}_2$ .<sup>61</sup> In our case, treatment under  $\text{H}_2$  diluted in argon (5 vol %) does not destabilize CoB up to 800 °C (Figure S7). Hence, temperature is not the only parameter explaining decomposition of CoB nanocrystals, but the atmosphere is important: strong reducing conditions are also required to form cobalt nanoparticles. On the other side, NiB undergoes decomposition when exposed to oxidizing conditions, through the formation of boron oxide. Metallic nickel is the major phase obtained and boron is irreversibly oxidized, as was already seen for CoB.<sup>19,61</sup> Our original observation is the generality of the decomposition of metal boride nanomaterials previously handled under air and moisture, when they are exposed to gas-phase treatment, in strongly oxidizing and reducing conditions.

In the catalytic hydrolysis of  $\text{NaBH}_4$  by cobalt–boron materials, the nature of the active site has been extensively discussed,<sup>21,22,27,36,61</sup> whether it is composed of cobalt only, cobalt and boron in an amorphous alloy, or one of the known crystalline cobalt–boron phases. Besides, boron (0.5 wt %) is known to act as a promoter of cobalt catalysts of the Fischer–Tropsch process by hindering coking.<sup>62</sup> Our results provide evidence for the instability of crystalline cobalt boride under a  $\text{H}_2$  atmosphere and at relatively low temperatures (400 °C) compared to the temperature of synthesis (750 °C), yielding metallic cobalt as the only cobalt species. Our results put also into perspective that the intrinsic activity of cobalt–boron materials in the hydrolysis of  $\text{NaBH}_4$  may result from its segregation to metallic cobalt nanoparticles. Indeed, Arzac et al.<sup>27</sup> highlighted the presence of cobalt particles through ex situ characterization in such systems. In the present study, NAP-XPS experiments unravel the true nature of the active surface composed of elemental cobalt, Co–O(H) in small proportions, and oxidized boron. Similar in situ studies applied to amorphous cobalt boride should provide useful information on the real active site in these systems, for which no consensus has been reached so far.<sup>22</sup> In the mechanism of  $\text{CO}_2$  methanation, the detection of Co–O(H) during in situ NAP-XPS is in favor of a steady state comprising partially oxidized cobalt. This is in accordance with previous works describing the dissociation of  $\text{CO}_2$  by cobalt through the formation of CoO.<sup>63</sup> Under the catalytic conditions of methanation, the surface concentration of oxidized cobalt might be even higher than that during NAP-XPS experiments (2 mbar) because the  $\text{CO}_2$  partial pressure is much higher (0.1 bar).

**Catalytic Activity of Metal Cobalt Nanoparticles Surrounded by Oxidized Boron.** Cobalt nanoparticles obtained from CoB decomposition during the  $\text{H}_2$  pretreatment are the actual active species catalyzing  $\text{CO}_2$  methanation. After  $\text{H}_2$  pretreatment, the size of the cobalt nanoparticles varies from 15 to 20 nm when supported on silicon dioxide ( $\text{SiO}_2$ ), according to the XRD data (Figure S6), in agreement with the particle sizes reported for cobalt nanoparticles supported on  $\text{SiO}_2$  and titanium dioxide ( $\text{TiO}_2$ ).<sup>64</sup> Interestingly, NAP-XPS in the B 1s region during exposure to  $\text{H}_2/\text{CO}_2$  indicates no specific species involving boron in the steady state.

The nature of the support onto which CoB was deposited has a drastic influence on the  $\text{CO}_2$  methanation reaction. CoB/

TiO<sub>2</sub> indeed shows a CH<sub>4</sub> production rate up to 5 times higher than that found on CoB/SiO<sub>2</sub> at a reaction temperature of 400 °C. The CH<sub>4</sub> production rates for the cobalt reference and the CoB-based/TiO<sub>2</sub> samples are of the same order of magnitude after almost 14 h on stream at 400 °C, in agreement with the formation of dispersed cobalt nanoparticles from segregation in the CoB precursor upon in situ exposure to H<sub>2</sub>. The continuous activity increase with the time on stream for TiO<sub>2</sub>-supported CoB at 400 °C should be related to reorganization of boron (hydr)oxide, leading to a better exposure of cobalt nanoparticles. Such a rearrangement could facilitate interactions between cobalt particles and the TiO<sub>2</sub> support. For cobalt-based catalytic materials, Riva et al. showed that TiO<sub>2</sub> favored the dispersion of cobalt nanoparticles during the reduction treatment thanks to metal–support interactions, while the cobalt particles sinter on SiO<sub>2</sub> due to the lack of significant interactions.<sup>60</sup> In the present case, TiO<sub>2</sub> might also favor dispersion of cobalt nanoparticles after elemental segregation occurred.

## CONCLUSION

To conclude, we have exploited in situ ensemble and local analyses to unravel the formation of metal nanoparticles upon exposure of nanocrystalline CoB to a reducing gas phase. Similarly, nickel borides decompose under oxidizing conditions. Such a decomposition at relatively low temperatures (400 °C) under a reactive atmosphere appears as a general process for metal borides obtained from the molten salt synthesis. In this process, boron is fully and irreversibly oxidized by oxygen species from the gas phase or from exposure to water and air prior to thermal treatment. Accordingly, our study points out strong morphological, chemical, and structural evolutions, which stress the special care that must be taken to attribute the measured properties, especially catalytic properties, to these crystalline materials. From these observations, the general instability of metal boride nanomaterials at relatively low temperatures (400 °C) under reactive atmospheres is questioned. By exploring with this study the stability ranges of boride nanomaterials, we delineate their acceptable ranges of study and application and we uncover the possible use of reducing atmospheres to exploit decomposition in boron compounds to yield complex materials.<sup>65</sup>

## EXPERIMENTAL SECTION

**Synthesis.** The reaction medium was prepared in an argon-filled glovebox (M-Braun). A total of 4 mmol of NaBH<sub>4</sub> (min 98%, Alfa Aesar) and 2 mmol of anhydrous CoCl<sub>2</sub> (99.99%, Alfa Aesar) were mixed with 5 g of a vacuum-dried LiCl/KCl mixture at the eutectic composition (45/55 wt %). The powders were finely ground in a ballmill (Retsch MM400) for 2 min at 20 Hz and then transferred into a glassy-carbon crucible. The crucible was maintained in a quartz tube, which was connected to an argon ramp. The medium was heated in a vertical oven (Carbolite) from RT to 750 °C (10 °C min<sup>-1</sup>) and maintained at 750 °C for 1.5 h. The medium was stirred with a glassy-carbon rod rotating at 100 rpm. After the apparatus cooled to RT, the frozen salt medium was washed with deionized water, the suspension was centrifuged for 15 min at 20 krpm (Nalgene), and the powder was separated from the supernatant. This washing procedure was repeated three times. The black powder was finally evacuated at 40 °C overnight.

**H<sub>2</sub> Reduction and H<sub>2</sub>/O<sub>2</sub> Oxidation Treatments.** A total of 50.6 mg of NiB powder (synthesis described in ref 6) was introduced into a continuous-flow quartz reactor. First, the powder was treated under 100 mL min<sup>-1</sup> of H<sub>2</sub> (1 atm) for 2 h at 500 °C. After cooling to RT, the sample was exposed four times to oxidation (120 mL min<sup>-1</sup> of a

H<sub>2</sub>/O<sub>2</sub>/helium mixture; volume ratio of 2:2:96; heating at 3 °C min<sup>-1</sup> from RT to 580 °C) and reduction treatments (115.2 mL min<sup>-1</sup> of a H<sub>2</sub>/helium mixture, volume ratio of 2:98, 3 °C min<sup>-1</sup> from RT to 500 °C and 2 h at 500 °C). H<sub>2</sub>, O<sub>2</sub>, and H<sub>2</sub>O concentrations were measured using a CP4900 microchromatograph (Varian).

**CO<sub>2</sub> Methanation. Supported CoB Materials.** A total of 40.0 mg of the cobalt boride powder was dispersed in deionized water and added dropwise to 360.0 mg of TiO<sub>2</sub>-P25 (Degussa) or SiO<sub>2</sub>-Aerosil 200 (Degussa; 10 nm nanoparticles; specific surface area of 200 m<sup>2</sup> g<sup>-1</sup>) suspended in deionized water during stirring. The resulting mixture was then sonicated in a USC100TH bath (VWR) for 5 min and stirred for 5 min three times. The dispersion was dried using a rotary evaporator (Büchi) at 60 °C. The reference-supported cobalt material was obtained from Co<sub>3</sub>O<sub>4</sub> supported on TiO<sub>2</sub>. This precursor was synthesized by the following procedure: 341.3 mg of Co(NO<sub>3</sub>)<sub>2</sub>·6H<sub>2</sub>O was dissolved in deionized water and added dropwise to 735.8 mg of TiO<sub>2</sub>-P25 (Degussa) suspended in deionized water during stirring. The suspension was stirred for 48 h at RT and then dry-  
evaporated at 95 °C. The powder was then annealed at 500 °C during 20 h in air.

**Methanation Experiments.** A total of 200 mg of precatalyst with particle sizes between 100 and 315 μm was loaded into a continuous-flow fixed-bed reactor and reduced in situ at 400 °C for 2 h under 30 mL min<sup>-1</sup> of H<sub>2</sub> (1 atm) prior to the catalytic reaction. The reaction was carried out at 1 atm from 200 to 500 °C under a reaction mixture composed of CO<sub>2</sub>/H<sub>2</sub>/helium (1:4:5 volume ratio) at 20 mL min<sup>-1</sup>. The exhaust gases were quantified using a gas chromatograph (Varian CP3800), equipped with Hayesep Q, Molsieve 5 Å, and CP-Sil-5CB columns. The reactants and products were detected with a flame ionization detector (CH<sub>4</sub>) and a thermal conductivity detector (CO and CO<sub>2</sub>). The exhaust gases were analyzed every 19 min with ~1% (relative) accuracy for the CH<sub>4</sub> production rate (moles of CH<sub>4</sub> produced per gram of cobalt per second). All transfer lines were maintained at 110 °C to avoid water condensation.

**In Situ TEM.** STEM-HAADF and environmental TEM were performed at the Institut de Physique et de Chimie of Strasbourg on a 200 kV JEOL 2100 F instrument [METSA (Microscopie Electronique et Sonde Atomique) national network] equipped with a Cs probe corrector, allowing one to achieve spatial resolutions down to 0.11 nm. For environmental TEM, the sample was exposed to a continuous 0.01 mL min<sup>-1</sup> gas flow. The sample holder was an Atmosphere model from Protochips able to withstand pressures of up to 1 atm and temperatures of up to 1000 °C (±3 °C and with high heating/cooling speeds of 50 °C s<sup>-1</sup>) under gas flow. These severe conditions do not alter the microscope performances in terms of spatial and energy resolution. The main drawback of the environmental TEM is electron beam damage, which may impact the microstructural changes within the region of interest during the treatment. To overcome this, specimen exposure to the electron beam was minimized, by carrying out all preliminary alignments away from the areas examined during the tests.

**XPS.** Most XPS experiments were performed on the NAP-XPS end station (SPECS) on the TEMPO beamline of the Synchrotron SOLEIL (Gif sur Yvette Cedex, France). The hemispheric electron analyzer was a Phoibos 150 NAP apparatus (SPECS). The samples were prepared by the dip-coating technique using a dip-coater (SolGelWay). Nanoparticles suspended in ethanol (30 mg mL<sup>-1</sup>) were deposited on a silicon wafer coated with a 50-nm-thick gold layer. The XPS spectra were calibrated according to the Au 4f<sub>7/2</sub> signal at 84.0 eV. Data analysis was performed on the CasaXPS software. Peaks were fitted using GL(30) component line shapes with linear (B 1s and O 1s) and Shirley (Co 2p<sub>3/2</sub> and Au 4f<sub>7/2</sub>) background types. The BE and full width at half-maximum (BE, eV; fwhm, eV) of the contributions are as follows: (i) in the B 1s region, CoB (187.9, 1.8), B<sup>0</sup> (189.2, 2.0), BO<sub>2</sub> (193.0, 2.1), BO<sub>3</sub> (195.4, 2.2), and the high-BE BO<sub>3</sub> species (197.1, 1.5) and (198.1, 2.5); (ii) in the O 1s region, Co–O(H) (532.0, 2.3), BO<sub>2</sub> (533.0, 2.4), BO<sub>3</sub> (534.9, 2.4), CO<sub>2</sub> (537.4, 1.3), and the high-BE BO<sub>3</sub> species (536.9, 1.4) and (537.9, 2.3). The spectrum recorded at 1500 eV was obtained on an Omicron Technology apparatus at the IMPC. It was equipped with a hemispheric analyzer

(SPECS) and an aluminum cathode with an Al K $\alpha$  monochromator. In this case, the XPS spectrum was calibrated according to the C 1s signal at 285.0 eV. The depth of XPS analysis in each region was evaluated by calculating the inelastic mean-free path of electrons extracted with a given kinetic energy from a given material.<sup>66</sup> Because the superficial layer is mainly composed of boron and oxygen, it is approximated to boron oxide for the calculations (considering that only boron yields similar values).

**NEXAFS.** NEXAFS spectra were recorded on the TEMPO beamline at Synchrotron SOLEIL (see above) in the total electron yield mode. The studied energy windows were as follows: (i) B K-edge, 185–205 eV with 0.1 eV steps and 205–220 eV with 0.2 eV steps; (ii) O K-edge, 525–530 eV with 0.2 eV steps, 530–540 eV with 0.1 eV steps, and 540–555 eV with 0.2 eV steps; (iii) Co L-edge, 770–774 eV with 0.2 eV steps, 774–785 eV with 0.1 eV steps, and 785–810 eV with 0.2 eV steps.

## ■ ASSOCIATED CONTENT

### 📄 Supporting Information

The Supporting Information is available free of charge on the ACS Publications website at DOI: [10.1021/acs.inorgchem.7b01279](https://doi.org/10.1021/acs.inorgchem.7b01279).

Characterization methods and Figures S1–S7 (PDF)

## ■ AUTHOR INFORMATION

### Corresponding Author

\*E-mail: [david.portehault@upmc.fr](mailto:david.portehault@upmc.fr).

### ORCID

Damien P. Debecker: 0000-0001-6500-2996

Cyril Thomas: 0000-0003-4224-6095

David Portehault: 0000-0003-4914-4913

### Present Addresses

<sup>‡</sup>G.G.: Institut de Chimie de la Matière Condensée de Bordeaux-CNRS, 33607 Pessac Cedex, France.

<sup>§</sup>S.M.: Groupe de Physique des Matériaux, University of Rouen, CNRS, France.

### Notes

The authors declare no competing financial interest.

## ■ ACKNOWLEDGMENTS

The authors acknowledge Patricia Beaunier from the Institut des Matériaux de Paris Centre for HRTEM and Domitille Giaume from the Institut de Recherche de Chimie Paris for ICP-OES. This work has been funded by the Ministère de l'Enseignement Supérieur et de la Recherche. The experiments at the TEMPO beamline at Synchrotron SOLEIL have been funded by SOLEIL under the User Proposal 20140081. CNRS, Sorbonne Universités, UPMC, Collège de France, and the METSA network are acknowledged for financial support.

## ■ REFERENCES

- (1) Terlan, B.; Levin, A.; Börrnert, F.; Simon, F.; Oschatz, M.; Schmidt, M.; Cardoso-Gil, R.; Lorenz, T.; Baburin, I.; Joswig, J.-O.; et al. Effect of Surface Properties on the Microstructure, Thermal and Colloidal Stability of VB<sub>2</sub> Nanoparticles. *Chem. Mater.* **2015**, *27*, 5106–5115.
- (2) Mattox, T. M.; Agrawal, A.; Milliron, D. J. Low Temperature Synthesis and Surface Plasmon Resonance of Colloidal Lanthanum Hexaboride (LaB<sub>6</sub>) Nanocrystals. *Chem. Mater.* **2015**, *27*, 6620–6624.
- (3) Rades, S.; Kornowski, A.; Weller, H.; Albert, B. Wet-Chemical Synthesis of Nanoscale Iron Boride, XAFS Analysis and Crystallisation to  $\alpha$ -FeB. *ChemPhysChem* **2011**, *12*, 1756–1760.

- (4) Rades, S.; Kraemer, S.; Seshadri, R.; Albert, B. Size and Crystallinity Dependence of Magnetism in Nanoscale Iron Boride,  $\alpha$ -FeB. *Chem. Mater.* **2014**, *26*, 1549–1552.

- (5) Portehault, D.; Devi, S.; Beaunier, P.; Gervais, C.; Giordano, C.; Sanchez, C.; Antonietti, M. A General Solution Route toward Metal Boride Nanocrystals. *Angew. Chem., Int. Ed.* **2011**, *50*, 3262–3265.

- (6) Gouget, G.; Beaunier, P.; Portehault, D.; Sanchez, C. New Route toward Nanosized Crystalline Metal Borides with Tunable Stoichiometry and Variable Morphologies. *Faraday Discuss.* **2016**, *191*, 511–525.

- (7) Carenco, S.; Portehault, D.; Boissière, C.; Mézailles, N.; Sanchez, C. 25th Anniversary Article: Exploring Nanoscaled Matter from Speciation to Phase Diagrams: Metal Phosphide Nanoparticles as a Case of Study. *Adv. Mater.* **2014**, *26*, 371–390.

- (8) Carenco, S.; Portehault, D.; Boissière, C.; Mézailles, N.; Sanchez, C. Nanoscaled Metal Borides and Phosphides: Recent Developments and Perspectives. *Chem. Rev.* **2013**, *113*, 7981–8065.

- (9) Nagamatsu, J.; Nakagawa, N.; Muranaka, T.; Zenitani, Y.; Akimitsu, J. Superconductivity at 39 K in Magnesium Diboride. *Nature* **2001**, *410*, 63–64.

- (10) Mori, T. Novel Physical Properties of Rare Earth Higher Borides. *J. Phys. Conf. Ser.* **2009**, *176*, 12036.

- (11) Albert, B.; Hillebrecht, H. Boron: Elementary Challenge for Experimenters and Theoreticians. *Angew. Chem., Int. Ed.* **2009**, *48*, 8640–8668.

- (12) Levine, J. B.; Tolbert, S. H.; Kaner, R. B. Advancements in the Search for Superhard Ultra-Incompressible Metal Borides. *Adv. Funct. Mater.* **2009**, *19*, 3519–3533.

- (13) Mohammadi, R.; Lech, A. T.; Xie, M.; Weaver, B. E.; Yeung, M. T.; Tolbert, S. H.; Kaner, R. B. Tungsten Tetraboride, an Inexpensive Superhard Material. *Proc. Natl. Acad. Sci. U. S. A.* **2011**, *108*, 10958–10962.

- (14) Lech, A. T.; Turner, C. L.; Mohammadi, R.; Tolbert, S. H.; Kaner, R. B. Structure of Superhard Tungsten Tetraboride: A Missing Link between MB<sub>2</sub> and MB<sub>12</sub> Higher Borides. *Proc. Natl. Acad. Sci. U. S. A.* **2015**, *112*, 3223–3228.

- (15) Mattox, T. M.; Chockkalingam, S.; Roh, I.; Urban, J. J. Evolution of Vibrational Properties in Lanthanum Hexaboride Nanocrystals. *J. Phys. Chem. C* **2016**, *120*, 5188–5195.

- (16) Mohammadi, R.; Turner, C. L.; Xie, M.; Yeung, M. T.; Lech, A. T.; Tolbert, S. H.; Kaner, R. B. Enhancing the Hardness of Superhard Transition-Metal Borides: Molybdenum-Doped Tungsten Tetraboride. *Chem. Mater.* **2016**, *28*, 632–637.

- (17) Yeung, M. T.; Lei, J.; Mohammadi, R.; Turner, C. L.; Wang, Y.; Tolbert, S. H.; Kaner, R. B. Superhard Monoborides: Hardness Enhancement through Alloying in W<sub>1-x</sub>Ta<sub>x</sub>B. *Adv. Mater.* **2016**, *28*, 6993–6998.

- (18) Akopov, G.; Yeung, M. T.; Kaner, R. B. Rediscovering the Crystal Chemistry of Borides. *Adv. Mater.* **2017**, *29*, 1604506.

- (19) Glavee, G. N.; Klabunde, K. J.; Sorensen, C. M.; Hadjapanayis, G. C. Borohydride Reductions of Metal Ions. A New Understanding of the Chemistry Leading to Nanoscale Particles of Metals, Borides, and Metal Borates. *Langmuir* **1992**, *8*, 771–773.

- (20) Liu, Y.-C.; Chen, Y.-W. Hydrogenation of p-Chloronitrobenzene on Lanthanum-Promoted NiB Nanometal Catalysts. *Ind. Eng. Chem. Res.* **2006**, *45*, 2973–2980.

- (21) Holbrook, K. A.; Twist, J. Hydrolysis of the Borohydride Ion Catalysed by Metal–boron Alloys. *J. Chem. Soc. A* **1971**, *0*, 890–894.

- (22) Demirci, U. B.; Miele, P. Cobalt in NaBH<sub>4</sub> Hydrolysis. *Phys. Chem. Chem. Phys.* **2010**, *12*, 14651–14665.

- (23) Vrubel, H.; Hu, X. Molybdenum Boride and Carbide Catalyze Hydrogen Evolution in Both Acidic and Basic Solutions. *Angew. Chem., Int. Ed.* **2012**, *51*, 12703–12706.

- (24) McCrory, C. C. L.; Jung, S.; Ferrer, I. M.; Chatman, S. M.; Peters, J. C.; Jaramillo, T. F. Benchmarking Hydrogen Evolving Reaction and Oxygen Evolving Reaction Electrocatalysts for Solar Water Splitting Devices. *J. Am. Chem. Soc.* **2015**, *137*, 4347–4357.

- (25) Masa, J.; Weide, P.; Peeters, D.; Sinev, I.; Xia, W.; Sun, Z.; Somsen, C.; Muhler, M.; Schuhmann, W. Amorphous Cobalt Boride (Co<sub>2</sub>B) as a Highly Efficient Nonprecious Catalyst for Electrochemical

Water Splitting: Oxygen and Hydrogen Evolution. *Adv. Energy Mater.* **2016**, *6*, 1502313–1502323.

(26) Park, H.; Encinas, A.; Scheifers, J. P.; Zhang, Y.; Fokwa, B. P. T. Boron-Dependency of Molybdenum Boride Electrocatalysts for the Hydrogen Evolution Reaction. *Angew. Chem., Int. Ed.* **2017**, *56*, 5575–5578.

(27) Arzac, G. M.; Rojas, T. C.; Fernández, A. Boron Compounds as Stabilizers of a Complex Microstructure in a Co-B-Based Catalyst for NaBH<sub>4</sub> Hydrolysis. *ChemCatChem* **2011**, *3*, 1305–1313.

(28) Chen, L.; Gu, Y.; Shi, L.; Yang, Z.; Ma, J.; Qian, Y. Synthesis and Oxidation of Nanocrystalline HfB<sub>2</sub>. *J. Alloys Compd.* **2004**, *368*, 353–356.

(29) Schaefer, Z. L.; Ke, X.; Schiffer, P.; Schaak, R. E. Direct Solution Synthesis, Reaction Pathway Studies, and Structural Characterization of Crystalline Ni<sub>3</sub>B Nanoparticles. *J. Phys. Chem. C* **2008**, *112*, 19846–19851.

(30) Terlan, B.; Levin, A. A.; Börrnert, F.; Zeisner, J.; Kataev, V.; Schmidt, M.; Eychmüller, A. A Size-Dependent Analysis of the Structural, Surface, Colloidal, and Thermal Properties of Ti<sub>1-x</sub>B<sub>2</sub>(x = 0.03–0.08) Nanoparticles. *Eur. J. Inorg. Chem.* **2016**, *2016*, 3460–3468.

(31) Hofmann, K.; Kalyon, N.; Kapfenberger, C.; Lamontagne, L.; Zarrini, S.; Berger, R.; Seshadri, R.; Albert, B. Metastable Ni<sub>7</sub>B<sub>3</sub>: A New Paramagnetic Boride from Solution Chemistry, Its Crystal Structure and Magnetic Properties. *Inorg. Chem.* **2015**, *54*, 10873–10877.

(32) Allard, L. F.; Overbury, S. H.; Bigelow, W. C.; Katz, M. B.; Nackashi, D. P.; Damiano, J. Novel MEMS-Based Gas-Cell/Heating Specimen Holder Provides Advanced Imaging Capabilities for In Situ Reaction Studies. *Microsc. Microanal.* **2012**, *18*, 656–666.

(33) Zhang, S.; Chen, C.; Cargnello, M.; Fornasiero, P.; Gorte, R. J.; Graham, G. W.; Pan, X. Dynamic Structural Evolution of Supported Palladium–Ceria Core–shell Catalysts Revealed by in Situ Electron Microscopy. *Nat. Commun.* **2015**, *6*, 7778.

(34) Starr, E.; Liu, Z.; Hävecker, M.; Knop-Gericke, A.; Bluhm, H. Investigation of Solid/vapor Interfaces Using Ambient Pressure X-Ray Photoelectron Spectroscopy. *Chem. Soc. Rev.* **2013**, *42*, 5833–5857.

(35) Choi, S.; Lapitan, L. D. S.; Cheng, Y.; Watanabe, T. Synthesis of Cobalt Boride Nanoparticles Using RF Thermal Plasma. *Adv. Powder Technol.* **2014**, *25*, 365–371.

(36) Wu, C.; Wu, F.; Bai, Y.; Yi, B.; Zhang, H. Cobalt Boride Catalysts for Hydrogen Generation from Alkaline NaBH<sub>4</sub> Solution. *Mater. Lett.* **2005**, *59*, 1748–1751.

(37) Sarma, D. D.; Santra, P. K.; Mukherjee, S.; Nag, A. X-Ray Photoelectron Spectroscopy: A Unique Tool To Determine the Internal Heterostructure of Nanoparticles. *Chem. Mater.* **2013**, *25*, 1222–1232.

(38) Carenco, S.; Tuxen, A.; Chintapalli, M.; Pach, E.; Escudero, C.; Ewers, T. D.; Jiang, P.; Borondics, F.; Thornton, G.; Alivisatos, A. P.; et al. Dealloying of Cobalt from CuCo Nanoparticles under Syngas Exposure. *J. Phys. Chem. C* **2013**, *117*, 6259–6266.

(39) Carenco, S.; Wu, C.-H.; Shavorskiy, A.; Alayoglu, S.; Somorjai, G. A.; Bluhm, H.; Salmeron, M. Synthesis and Structural Evolution of Nickel-Cobalt Nanoparticles Under H<sub>2</sub> and CO<sub>2</sub>. *Small* **2015**, *11*, 3045–3053.

(40) Polack, F.; Silly, M.; Chauvet, C.; Lagarde, B.; Bergeard, N.; Izquierdo, M.; Chubar, O.; Krizmancic, D.; Ribbens, M.; Duval, J.-P.; et al. TEMPO: A New Insertion Device Beamline at SOLEIL for Time Resolved Photoelectron Spectroscopy Experiments on Solids and Interfaces. *AIP Conf. Proc.* **2009**, *1234*, 185–188.

(41) Tissot, H.; Olivieri, G.; Gallet, J.-J.; Bourmel, F.; Silly, M. G.; Sirotti, F.; Rochet, F. Cation Depth-Distribution at Alkali Halide Aqueous Solution Surfaces. *J. Phys. Chem. C* **2015**, *119*, 9253–9259.

(42) Head, A. R.; Chaudhary, S.; Olivieri, G.; Bourmel, F.; Andersen, J. N.; Rochet, F.; Gallet, J.-J.; Schnadt, J. Near Ambient Pressure X-Ray Photoelectron Spectroscopy Study of the Atomic Layer Deposition of TiO<sub>2</sub> on RuO<sub>2</sub> (110). *J. Phys. Chem. C* **2016**, *120*, 243–251.

(43) Mavel, G.; Escard, J.; Costa, P.; Castaing, J. ESCA Surface Study of Metal Borides. *Surf. Sci.* **1973**, *35*, 109–116.

(44) Brundle, C. R.; Chuang, T. J.; Rice, D. W. X-Ray Photoemission Study of the Interaction of Oxygen and Air with Clean Cobalt Surfaces. *Surf. Sci.* **1976**, *60*, 286–300.

(45) Ennaceur, M. M.; Terreault, B. XPS Study of the Process of Oxygen Gettering by Thin Films of PACVD Boron. *J. Nucl. Mater.* **2000**, *280*, 33–38.

(46) Bellott, B. J.; Noh, W.; Nuzzo, R. G.; Girolami, G. S. Nanoenergetic Materials: Boron Nanoparticles from the Pyrolysis of Decaborane and Their Functionalisation. *Chem. Commun.* **2009**, 3214–3215.

(47) Riedel, T.; Schaub, G. Low-Temperature Fischer–Tropsch Synthesis on Cobalt Catalysts—Effects of CO<sub>2</sub>. *Top. Catal.* **2003**, *26*, 145–156.

(48) Hävecker, M.; Mayer, R. W.; Knop-Gericke, A.; Bluhm, H.; Kleimenov, E.; Liskowski, A.; Su, D.; Follath, R.; Requejo, F. G.; Ogletree, D. F.; et al. In Situ Investigation of the Nature of the Active Surface of a Vanadyl Pyrophosphate Catalyst during N-Butane Oxidation to Maleic Anhydride. *J. Phys. Chem. B* **2003**, *107*, 4587–4596.

(49) Pozdnyakova, O.; Teschner, D.; Woosch, A.; Kröhnert, J.; Steinhauer, B.; Sauer, H.; Toth, L.; Jentoft, F. C.; Knop-Gericke, A.; Paál, Z.; et al. Preferential CO Oxidation in Hydrogen (PROX) on Ceria-Supported Catalysts, Part II: Oxidation States and Surface Species on Pd/CeO<sub>2</sub> under Reaction Conditions, Suggested Reaction Mechanism. *J. Catal.* **2006**, *237*, 17–28.

(50) Virnovskaia, A.; Jørgensen, S.; Hafizovic, J.; Prytz, Ø.; Kleimenov, E.; Hävecker, M.; Bluhm, H.; Knop-Gericke, A.; Schlögl, R.; Olsbye, U. In Situ XPS Investigation of Pt(Sn)/Mg(Al)O Catalysts during Ethane Dehydrogenation Experiments. *Surf. Sci.* **2007**, *601*, 30–43.

(51) Behrens, M.; Studt, F.; Kasatkin, I.; Kuhl, S.; Hävecker, M.; Abild-Pedersen, F.; Zander, S.; Girgsdies, F.; Kurr, P.; Knief, B.-L.; et al. The Active Site of Methanol Synthesis over Cu/ZnO/Al<sub>2</sub>O<sub>3</sub> Industrial Catalysts. *Science* **2012**, *336*, 893–897.

(52) Alstrup, I.; Chorkendorff, I.; Candia, R.; Clausen, B. S.; Topsoe, H. A Combined X-Ray Photoelectron and Mossbauer Emission Spectroscopy Study of the State of Cobalt in Sulfided, Supported, and Unsupported Co-Mo Catalysts. *J. Catal.* **1982**, *77*, 397–409.

(53) Joyner, D. J.; Hercules, D. M. Chemical Bonding and Electronic Structure of B<sub>2</sub>O<sub>3</sub>, H<sub>3</sub>BO<sub>3</sub>, and BN: An ESCA, Auger, SIMS, and SXS Study. *J. Chem. Phys.* **1980**, *72*, 1095.

(54) Frazer, B. H.; Gilbert, B.; Sonderegger, B. R.; De Stasio, G. The Probing Depth of Total Electron Yield in the Sub-keV Range: TEY-XAS and X-PEEM. *Surf. Sci.* **2003**, *537*, 161–167.

(55) Li, D.; Bancroft, G. M.; Fleet, M. E. B K-Edge XANES of Crystalline and Amorphous Inorganic Materials. *J. Electron Spectrosc. Relat. Phenom.* **1996**, *79*, 71–73.

(56) Tuxen, A.; Carenco, S.; Chintapalli, M.; Chuang, C. H.; Escudero, C.; Pach, E.; Jiang, P.; Borondics, F.; Beberwyck, B.; Alivisatos, A. P.; et al. Size-Dependent Dissociation of Carbon Monoxide on Cobalt Nanoparticles. *J. Am. Chem. Soc.* **2013**, *135*, 2273–2278.

(57) Perry, D. L. *Handbook of Inorganic Compounds*, 2nd ed.; CRC Press, 2011.

(58) Carenco, S.; Sassoye, C.; Faustini, M.; Eloy, P.; Debecker, D. P.; Bluhm, H.; Salmeron, M. B. The Active State of Supported Ruthenium Oxide Nanoparticles during Carbon Dioxide Methanation. *J. Phys. Chem. C* **2016**, *120*, 15354–15361.

(59) Kim, A.; Sanchez, C.; Patriarche, G.; Ersen, O.; Moldovan, S.; Wisnet, A.; Debecker, D. P.; Sassoye, C. Selective CO<sub>2</sub> Methanation on Ru/TiO<sub>2</sub> Catalyst: Unraveling the Decisive Role of the TiO<sub>2</sub> Support Crystal Structure. *Catal. Sci. Technol.* **2016**, *6*, 8117–8128.

(60) Riva, R.; Miessner, H.; Vitali, R.; Del Piero, G. Metal–support Interaction in Co/SiO<sub>2</sub> and Co/TiO<sub>2</sub>. *Appl. Catal., A* **2000**, *196*, 111–123.

(61) Patel, N.; Fernandes, R.; Guella, G.; Kale, A.; Miotello, A.; Patton, B.; Zanchetta, C. Structured and Nanoparticle Assembled Co-B Thin Films Prepared by Pulsed Laser Deposition: A Very Efficient

Catalyst for Hydrogen Production. *J. Phys. Chem. C* **2008**, *112*, 6968–6976.

(62) Saeys, M.; Tan, K. F.; Chang, J.; Borgna, A. Improving the Stability of Cobalt Fischer–Tropsch Catalysts by Boron Promotion. *Ind. Eng. Chem. Res.* **2010**, *49*, 11098–11100.

(63) Lahtinen, J.; Anraku, T.; Somorjai, G. A. C, CO and CO<sub>2</sub> Hydrogenation on Cobalt Foil Model Catalysts: Evidence for the Need of CoO Reduction. *Catal. Lett.* **1994**, *25*, 241–255.

(64) Reuel, R. C.; Bartholomew, C. H. The Stoichiometries of H<sub>2</sub> and CO Adsorptions on Cobalt: Effects of Support and Preparation. *J. Catal.* **1984**, *85*, 63–77.

(65) McCue, I.; Benn, E.; Gaskey, B.; Erlebacher, J. Dealloying and Dealloyed Materials. *Annu. Rev. Mater. Res.* **2016**, *46*, 263–286.

(66) Tanuma, S.; Powell, C. J.; Penn, D. R. Calculations of Electron Inelastic Mean Free Paths. V. Data for 14 Organic compounds Over The 50–2000 eV Range. *Surf. Interface Anal.* **1994**, *21*, 165–176.